



Figures and figure supplements

Nicotinamide mononucleotide adenylyltransferase uses its NAD⁺ substrate-binding site to chaperone phosphorylated Tau

Xiaojuan Ma *et al*

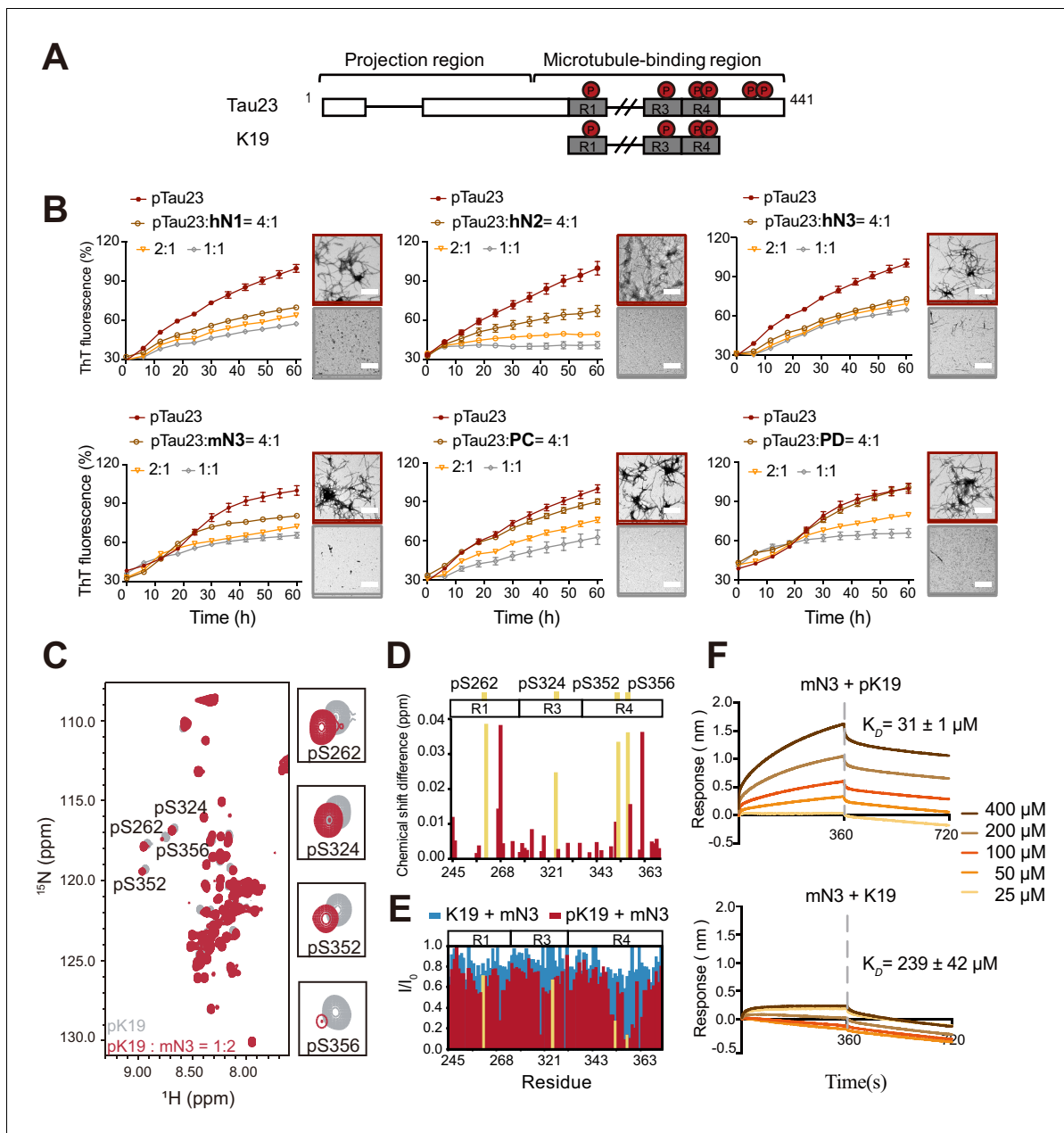


Figure 1. NMNATs inhibit pTau amyloid fibril formation and specifically bind to the phosphorylated sites of pTau. (A) Domain compositions of Tau23 and K19. The repeat regions are presented as gray boxes. Phosphorylation sites characterized in this work are marked. (B) Inhibition of NMNATs on the amyloid fibril formation of pTau23 (60 μM) by the ThT fluorescence kinetic assay and TEM microscopy. Human NMNATs: hN1, hN2, and hN3; *Drosophila* Nmnats: PC and PD; mouse NMNAT3: mN3. A gradient concentration of NMNATs were applied as indicated. The data showed correspond to mean \pm s.d., with $n = 5$. The EM images framed in red mean pTau23 only and those in gray mean 1:1 (mol: mol, pTau23:NMNAT). Scale bar: 500 nm. (C) Overlay of 2D ^1H - ^{15}N HSQC spectra of pK19 alone (100 μM , gray) and pK19 titrated by mN3 (200 μM , red). Signals of pSer residues are enlarged. (D) Residue-specific chemical shift changes of pK19 analyzed based on (c). The domain organization of K19 is indicated and signals of pSer residues are highlighted in yellow. (E) Residue-specific intensity changes of pK19 (red) and K19 signals (light blue) based on (c) and **Figure 1—figure supplement 6a**. (F) Binding affinity of pK19/K19 with mN3 measured by BLI. The association and dissociation profiles of pK19/K19 to mN3 (20 $\mu\text{g ml}^{-1}$) divided by a vertical dash line are shown. Concentrations of pK19/K19 proteins and dissociation constant (K_D) are indicated.

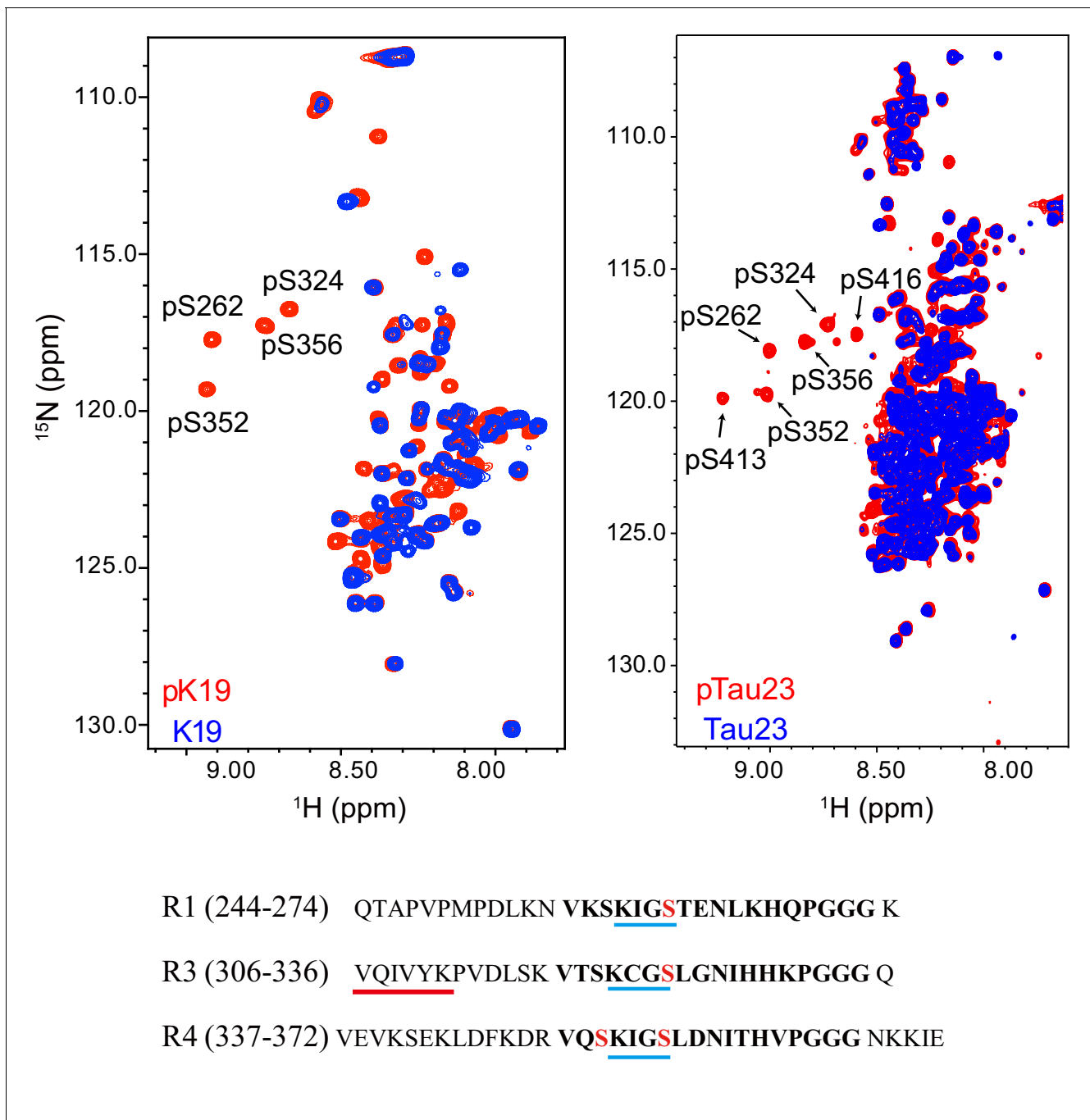


Figure 1—figure supplement 1. Characterization of MARK2 phosphorylation sites on pK19 (left) and pTau23 (right) by NMR. Overlay of the 2D ^1H - ^{15}N HSQC spectra of pK19 (red) and K19 (blue), and pTau23 (red) and Tau23 (blue). The phosphorylated serine residues are labeled. The primary sequences of R1, R3, and R4 are shown. The 18-residue repeats are in bold. The KXGS motifs are underscored with blue lines. The four serine residues that are phosphorylated by MARK2 are highlighted in red. The fibril-forming core sequence is underscored with a red line.

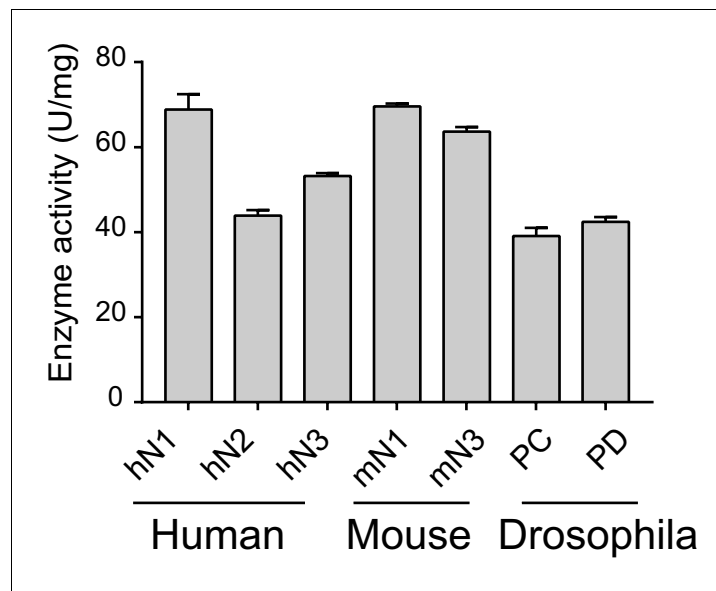


Figure 1—figure supplement 2. Enzyme activities of different isoforms of NMNAT from different organisms. The data shown correspond to mean \pm s.d., with $n = 3$.

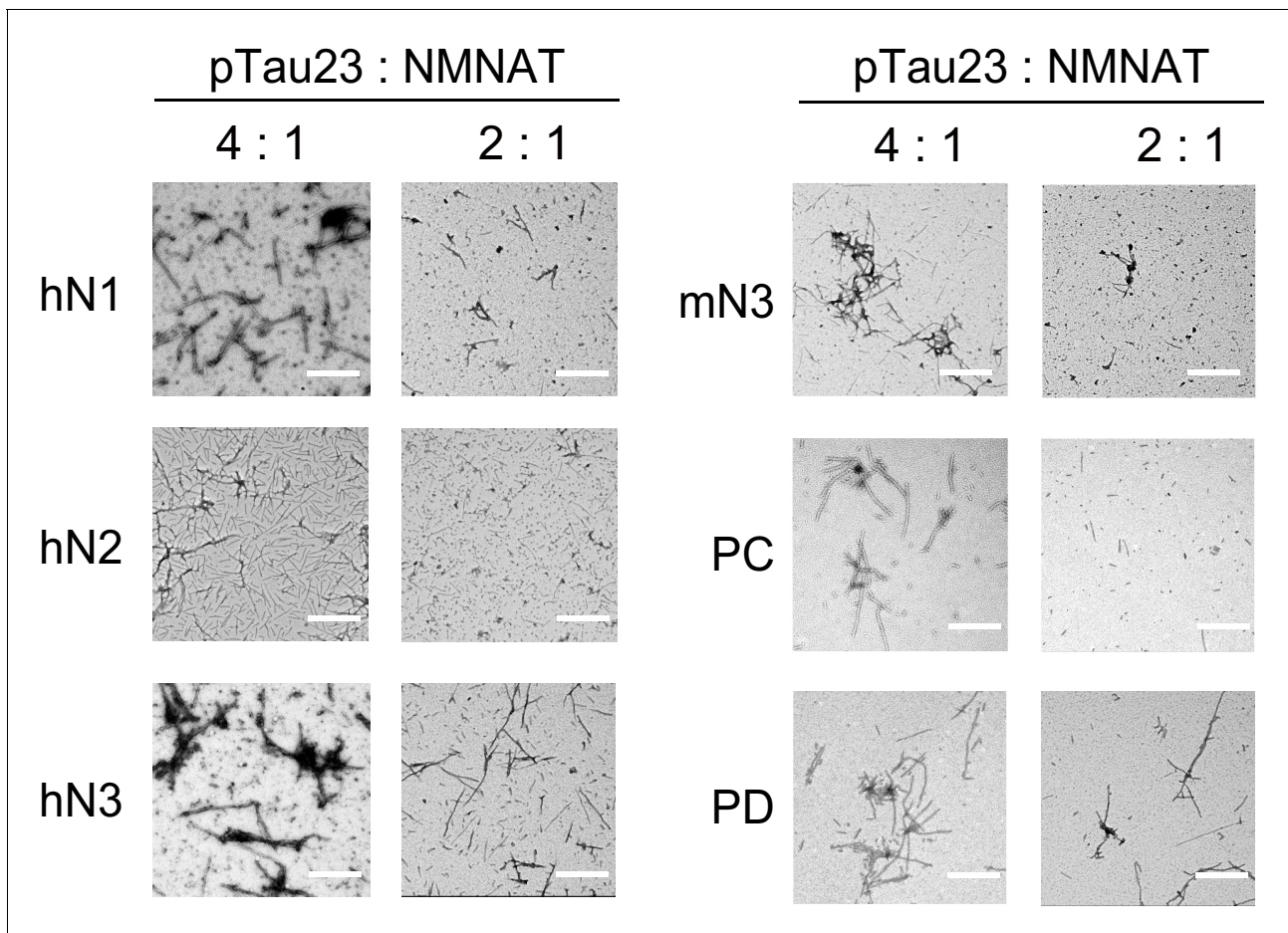


Figure 1—figure supplement 3. Inhibition of NMNATs on the fibril formation of pTau23 imaged by negative-staining TEM. Tau fibrils were imaged after pTau23 incubation with NMNATs at 37°C for 60 hr. The molar ratios of pTau23 to NMNATs are indicated. Scale bars: 500 nm.

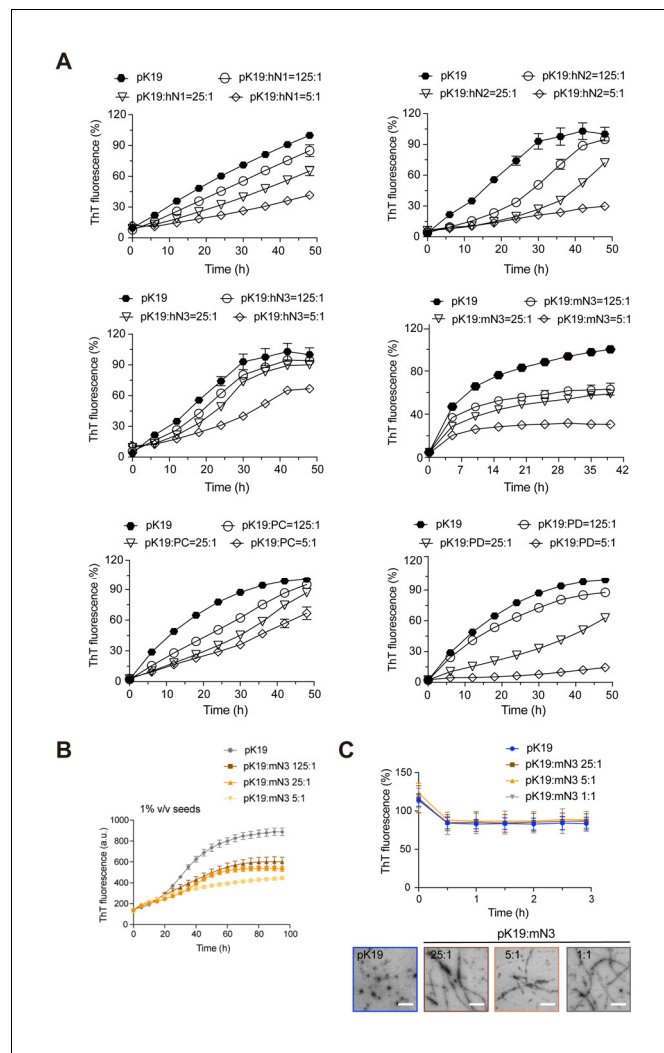


Figure 1—figure supplement 4. Inhibition of NMNATs on the fibril formation of pK19. (A) Inhibition of NMNATs on the amyloid fibril formation of pK19 (100 μ M) measured by the ThT fluorescence kinetic assay. A gradient concentration of NMNATs was applied as indicated. The data shown correspond to mean \pm s.d., with $n = 3$. (B) ThT fluorescent assay showed the inhibition of mN3 on the fibril formation of pK19 (100 μ M) in the presence of 1% (v/v) preformed pK19 fibril seeds. Molar ratios of pK19 to mN3 are indicated. The data shown correspond to mean \pm s.d., with $n = 5$. (C) mN3 exhibits no disaggregation of preformed pK19 fibrils measured by ThT fluorescence assay (upper). The molar ratios of pK19 to mN3 are indicated. Error bars correspond to mean \pm s.d., with $n = 3$. TEM images (lower) show no effect of mN3 on preformed pK19 fibrils. pK19 samples were imaged by TEM after incubation with indicated concentrations of mN3 at 37°C for 3 hr. Scale bars: 500 nm.

		TXXH catalysis motif			WXXT NMN binding motif	
NMNAT3 [Homo]	1	MKSRI P---VLLA CGSFNP	TNM HL	RMFEVARD HLHQTMGYQV IQGIIISPVD TYG KKDL LAAS HHRVAMARLA LQTSDWIRVD PWEESEA WM ET KVLRHHH		
NMNAT3 [Mus]	1	MKNRI P---VLLA CGSFNP	TNM HL	RLFEVARD HLHQTGRYQV IEGIIISPVD SYG KKDL VAS HHRVAMARLA LQTSDWIRVD PWEESEA WM ET KVLRHHH		
IsoformD[Drosop]	5	IEETK SLLPRIAFIA CGCFSP	TPM HL	RMFEIAKD HFEMQGTTHR VGGIISPETH SYG KKGL ASA LDRCAMVCLA TQSSNWIRLS DWEVHQ WM RT AVLQHHQ		
IsoformC[Drosop]	5	IEETK SLLPRIAFIA CGCFSP	TPM HL	RMFEIAKD HFEMQGTTHR VGGIISPETH SYG KKGL ASA LDRCAMVCLA TQSSNWIRLS DWEVHQ WM RT AVLQHHQ		
NMNAT1 [Homo]	1	MENSE --KTEVLLA CGSFNP	TNM HL	RLFELAKD YMNGTGRTV VGGIISPVD AYK KKGL LIPA YHRVIMAE LA TKNSKWVEVD TWESLQ WK ET KVLRHHQ		
NMNAT1 [Mus]	1	MDSSK --KTEVLLA CGSFNP	TNM HL	RLFELAKD YMHATGKYSV IKGIIISPVD AYK KKGL LIPA HHRVIMAE LA TKNSHWVEVD TWESLQ WK ET KVLRHHQ		
NMNAT2 [Homo]	1	MTETT K--THVILLA CGSFNP	TKG HI	MPFERARD YLHKTGRFIV IGGIVSPVHD SYG QQLV SS RHRLIMCQLA VQNSDWIRVD PWECYQ WQ TT SVLEHHR		
NMNAT2 [Mus]	1	MTETT K--THVILLA CGSFNP	TKG HI	MPFERARD YLHKTGRFIV IGGIVSPVHD SYG QQLV SS RHRLIMCQLA VQNSDWIRVD PWECYQ WQ TT SVLEHHR		
NMNAT3 [Homo]	173	KG YIAE SPILRMHQHN IHLAKEPVQN	EISATYI	RKAL RGQ-S VKYLIPDAVI TYIKDHGLYT KGSTWKGKST QS----- 246 252		
NMNAT3 [Mus]	172	ERYISD SPILQQFQHN IHLAREPVLN	EISATYV	RKAL RGQ-S VKYLLPEAVI TYIRDQGLYI NDGSWKGK-- 241 245		
IsoformD[Drosop]	191	GKFIFD SDILTKYQSN ITLITNWVPN	EVSSSTLI	RRLL RGQ-S VKYLLDDLVL EYIKRQRLFN FKSR---DAP AP----- 261 266		
IsoformC[Drosop]	191	GKFIFD SDILTKYQSN ITLITNWVPN	EVSSSTLI	RRLL RGQ-S VKYLLDDLVL EYIKRQRLFN FKSKYITDAV RPNHLLFNHA 272 358		
NMNAT1 [Homo]	194	QKFIYE SDVLWKHRSN IHVVNEWIAN	DISSTKI	RKAL RRGQ-S IRYLVPDLVQ EYIEKHNLVS SESEDRNAGV ILAP----- 269 279		
NMNAT1 [Mus]	194	QKFIYE SDVLWRHQSN IHLVNEWITN	DISSTKI	RKAL RRGQ-S IRYLVPDLVQ EYIEKHELYN TESEGRNAGV TLAP----- 270 285		
NMNAT2 [Homo]	238	DRIMNH SSILRKYKNN IMVVKDDINH	VVSSSTKS	RLAL RHGDGH VVDYLSQPVI DYILKSQLYI NASG----- 307 307		
NMNAT2 [Mus]	238	DRIMNH SSILRKYKNN IMVVKDDINH	VVSSSTKS	RLAL RHGDGH VVDYLSQPVI DYILKSQLYI NASG----- 307 307		
ISSTXXR ATP binding motif						

Figure 1—figure supplement 5. Sequence alignment of NMNATs from different species. The catalytic and substrate-binding motifs (highlighted with orange frames) are highly conserved and the conserved residues are in blue. The positively charged residues that are essential for the chaperone-like activity are colored in red.

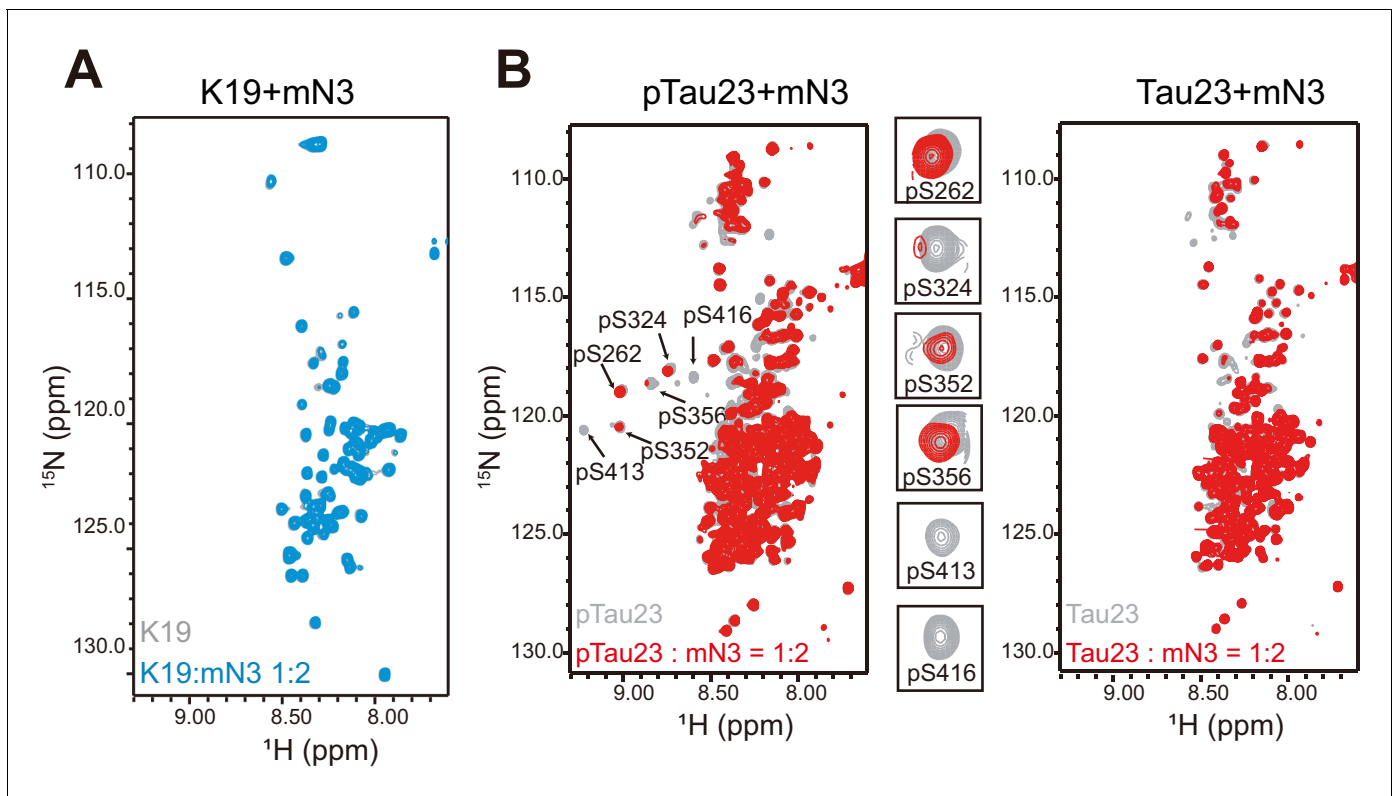


Figure 1—figure supplement 6. NMR titration of NMNAT to Tau. (A) Overlay of 2D ^1H - ^{15}N HSQC spectra of K19 alone (100 μM , gray) and K19 titrated by mN3 (blue; molar ratio 1:2). (B) Overlay of 2D ^1H - ^{15}N HSQC spectra of pTau23 (left)/Tau23(right) alone (100 μM , gray) and that titrated by mN3 (red; molar ratio 1:2). pSer residues are enlarged.

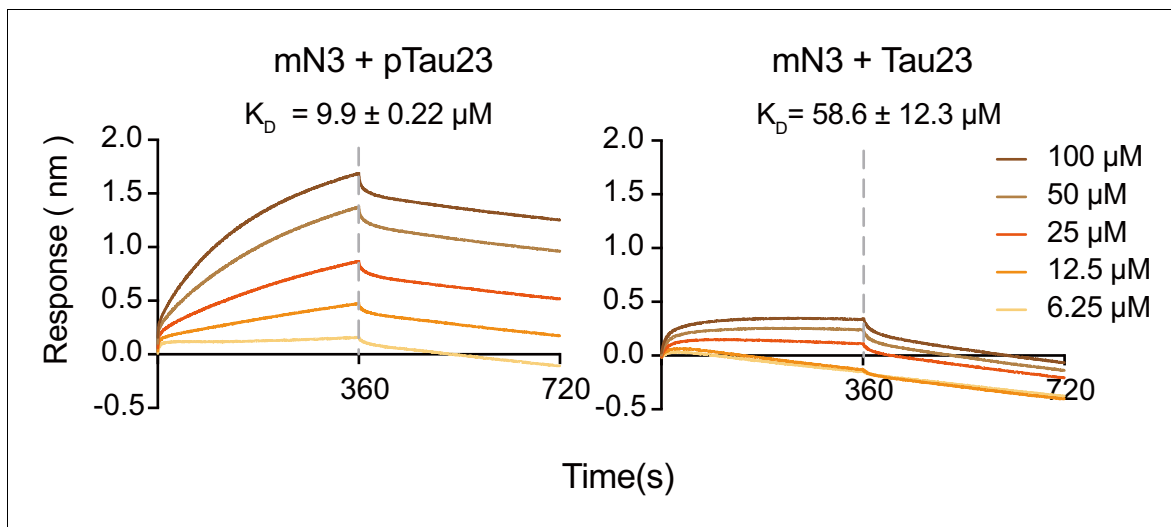


Figure 1—figure supplement 7. Binding affinity of pTau23 (left) and Tau23 (right) with mN3 measured by BLI. The SA sensor chip was coated with biotinylated mN3 ($20 \mu\text{g ml}^{-1}$). The association and dissociation profiles divided by a vertical dash line are shown. The K_D values are reported.

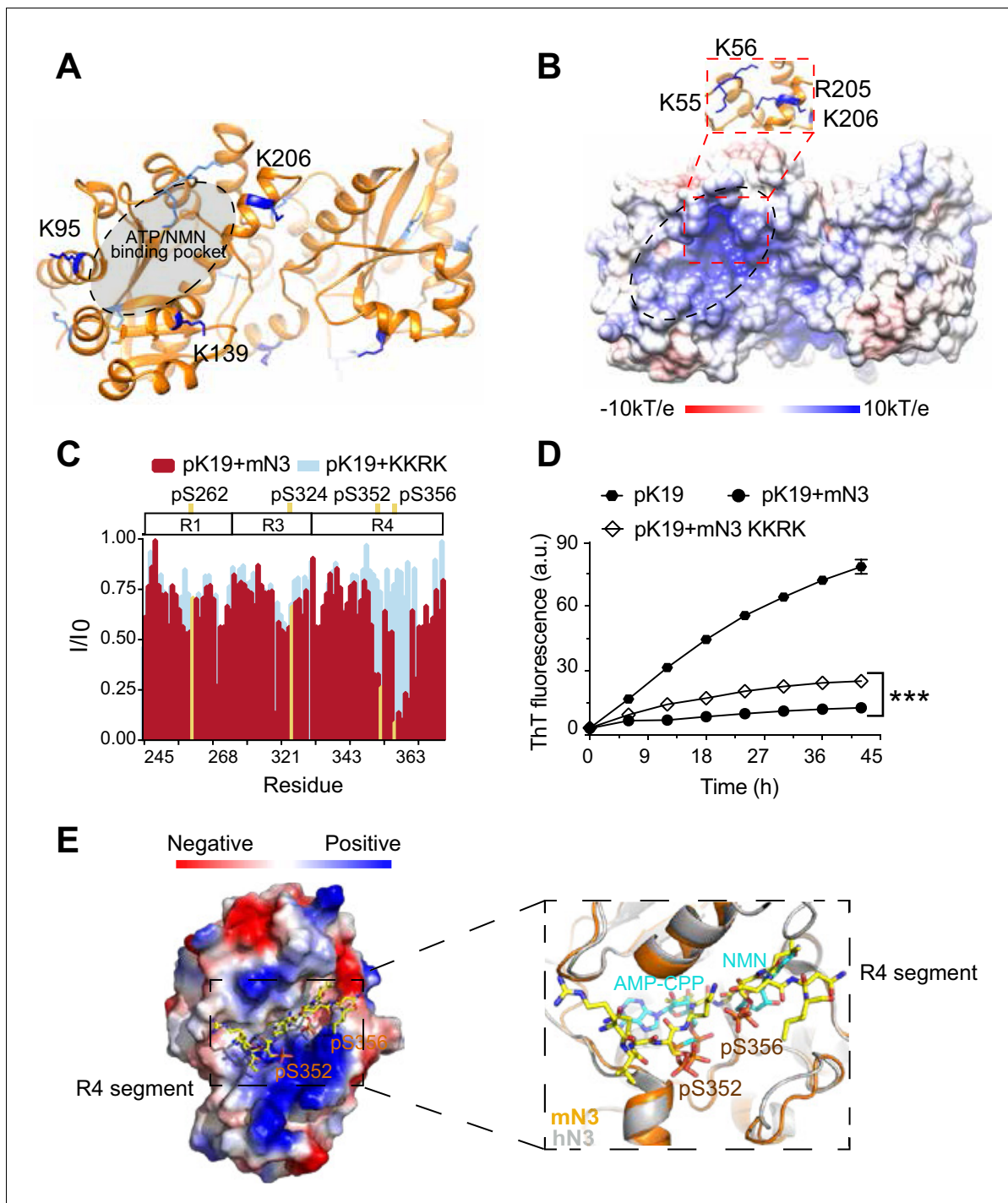


Figure 2. Structural characterization of the pTau-binding site on mN3. (A) The structure of mN3 is shown in cartoon. Lysine residues that cross-linked with pK19 are shown as sticks in dark blue. Other lysine residues of mN3 are shown in light blue. The ATP/NMN binding site is shaded in gray. (B) Electrostatic surface representation of mN3. The *pqr* file was calculated at pH = 6.5. The positively-charged patch is highlighted with dash lines. The residues that compose the positively charged patch are shown as sticks in blue in the zoom-in view. (C) Overlay of the residue-specific intensity changes of pK19 signals titrated by mN3 (red) and KKRK mutant (light blue), respectively. pSer residues are colored in yellow. The domain organization of K19 is indicated on top. (D) Influence of KKRK mutations on the inhibition of mN3 against pK19 amyloid aggregation measured by the ThT fluorescence assays. The molar ratio of pK19 to mN3 is 1:0.2. Data correspond to mean \pm s.d., with $n = 3$. Values are compared using Student's *t*-test. *** $p < 0.001$. (E) Structural model of mN3 in complex with the phosphorylated R4 segment ³⁴⁹RVQ(p)SKIG(p)SLDNI³⁶⁰. The electrostatic surface of the mN3 structure is shown. The peptide is shown as sticks in yellow. A zoom-in view of the peptide-binding site in (E) superimposed on the structure of hN3 in complex with AMP-CPP and NMN (PDB ID: 1NUS). AMP-CPP and NMN are shown as sticks in cyan.

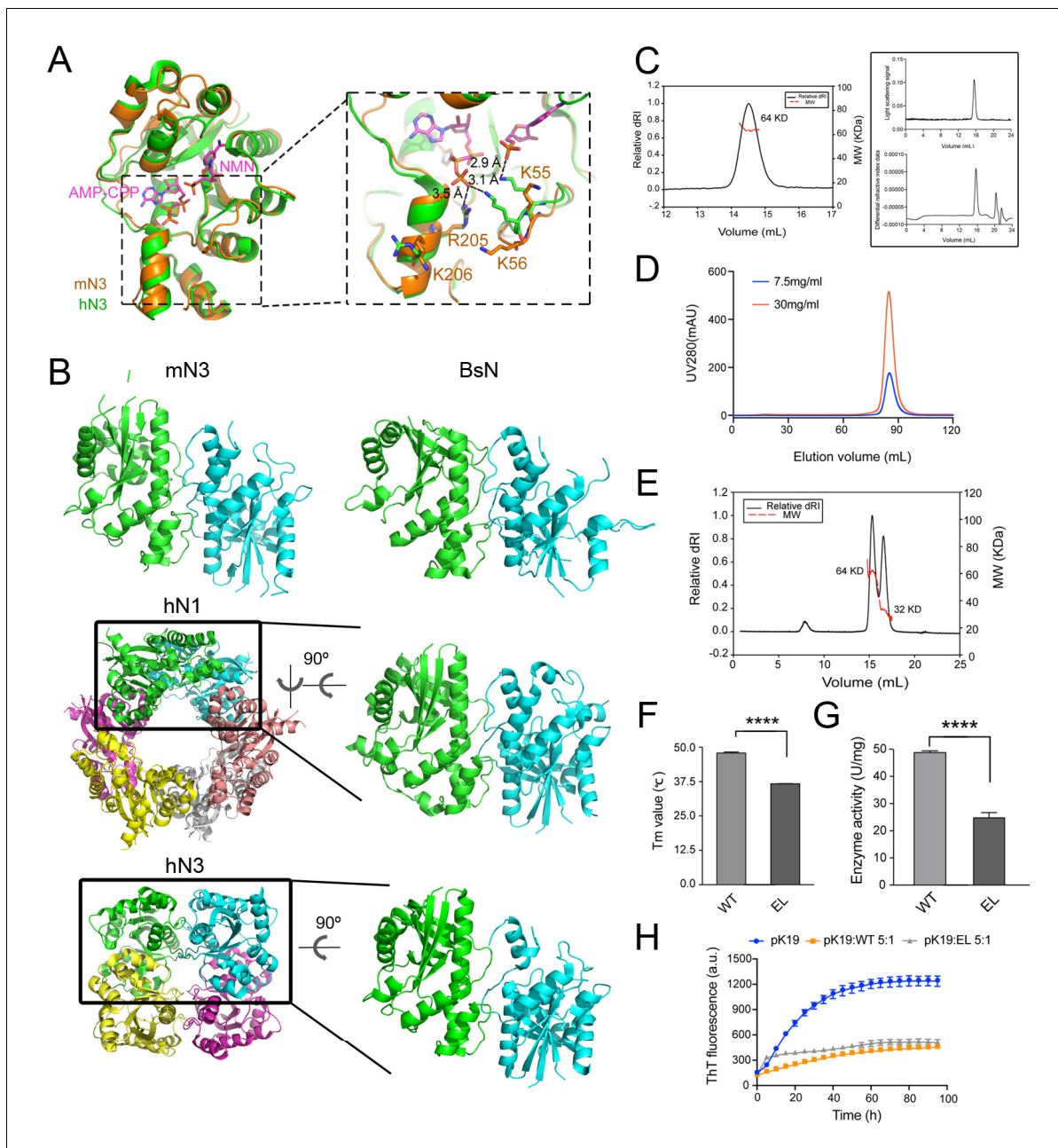


Figure 2—figure supplement 1. Characterization of mN3 dimer structure and activities. (A) Structure superimposition of mN3 (orange) and hN3 (green, PDB ID: 1NUS). Substrates AMP-CPP (non-hydrolyzable ATP analog) and NMN from the structure of hN3 are shown as sticks in magenta. Positively charged residues that compose the positively-charged patch of mN3 are shown in sticks. Their interactions with the phosphate groups of substrates are labeled in the zoom-in view. (B) Structures of NMNAT proteins. Functional oligomers are shown including dimers of mN3 (PDB ID: 5Z9R) and BsN (1KAM), hexamer of hN1 (1KQN) and tetramer of hN3 (1NUR). The conserved dimer units (green and cyan) are shown in the same orientation. (C) SEC-MALS of mN3. The graph on the left shows the elution profile of mN3 by size exclusion chromatography (smooth trace) and the resulting molecular mass (red dotted line). Raw data of light scattering signal (upper) and dRI (lower) are shown on the right. (D) Size exclusion chromatography of mN3 at indicated concentrations. (E) SEC-MALS of mN3 EL mutant. The resulting molecular mass indicates a mixture of mN3 dimer and monomer in solution. (F) Melting temperature of mN3 WT and EL mutant measured by the DSF assay. The data shown correspond to mean \pm s.d., with $n = 3$. Values are compared using Student's t-test. **** $p < 0.0001$. (G) Enzyme activities of mN3 WT and EL mutant measured with the NMN concentration of $625 \mu\text{M}$. The data shown correspond to mean \pm s.d., with $n = 3$. Values are compared using Student's t-test. **** $p < 0.0001$. (H) ThT kinetic assay of pK19 ($100 \mu\text{M}$) inhibited by mN3 WT and EL mutant. The molar ratio of pK19 to mN3 is indicated. The data shown correspond to mean \pm s.d., with $n = 5$.

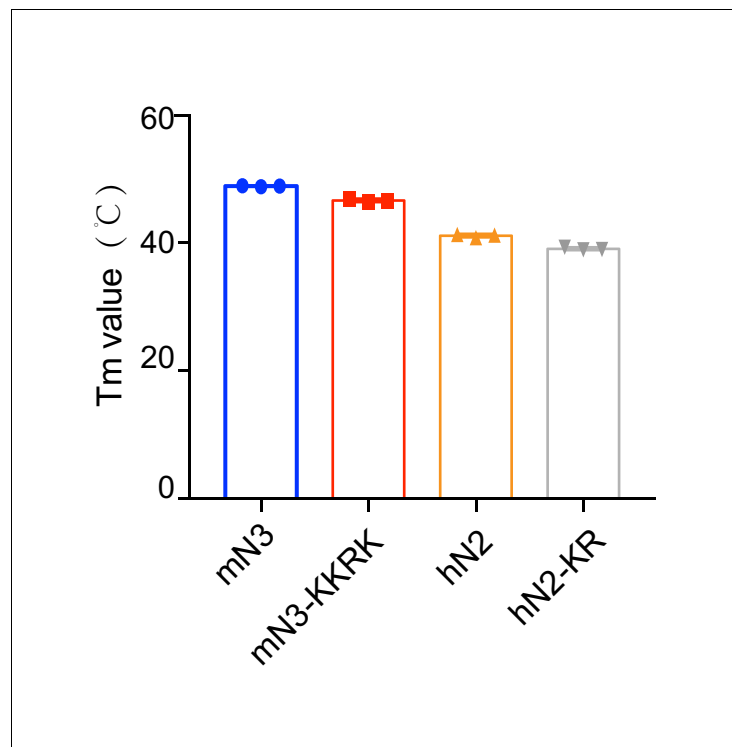


Figure 2—figure supplement 2. Melting temperature of mN3 and hN2 variants measured by the DSF assay. The data shown correspond to mean \pm s.d., with $n = 3$.

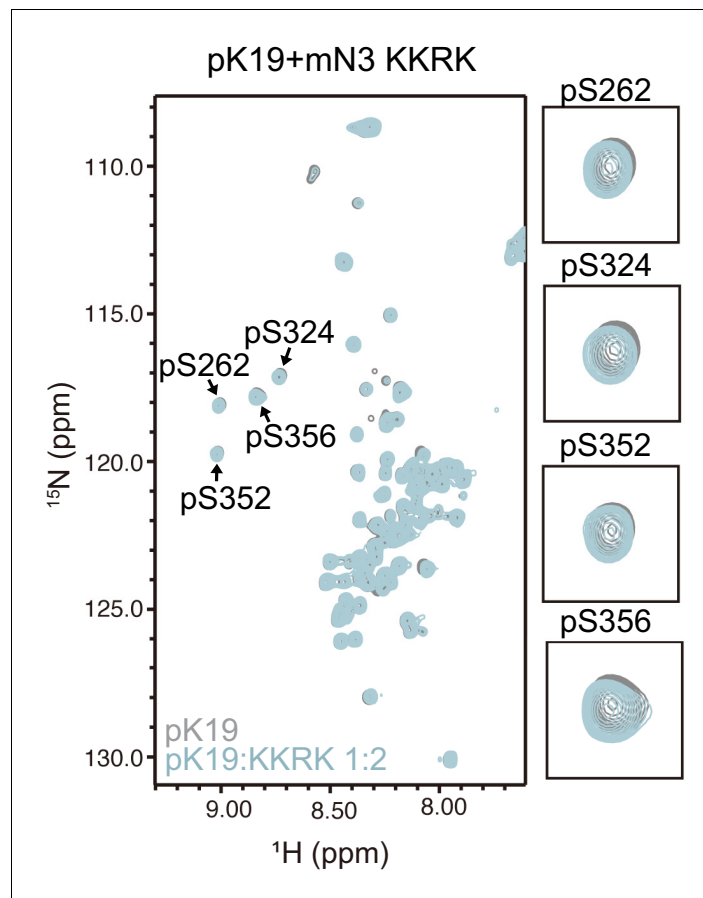


Figure 2—figure supplement 3. 2D ^1H - ^{15}N HSQC spectra of pK19 titrated by mN3-KKRK. pK19: 100 μM , gray; pK19 titrated by mN3-KKRK: molar ratio of 1:2, light blue. Signals of pSer residues are enlarged.

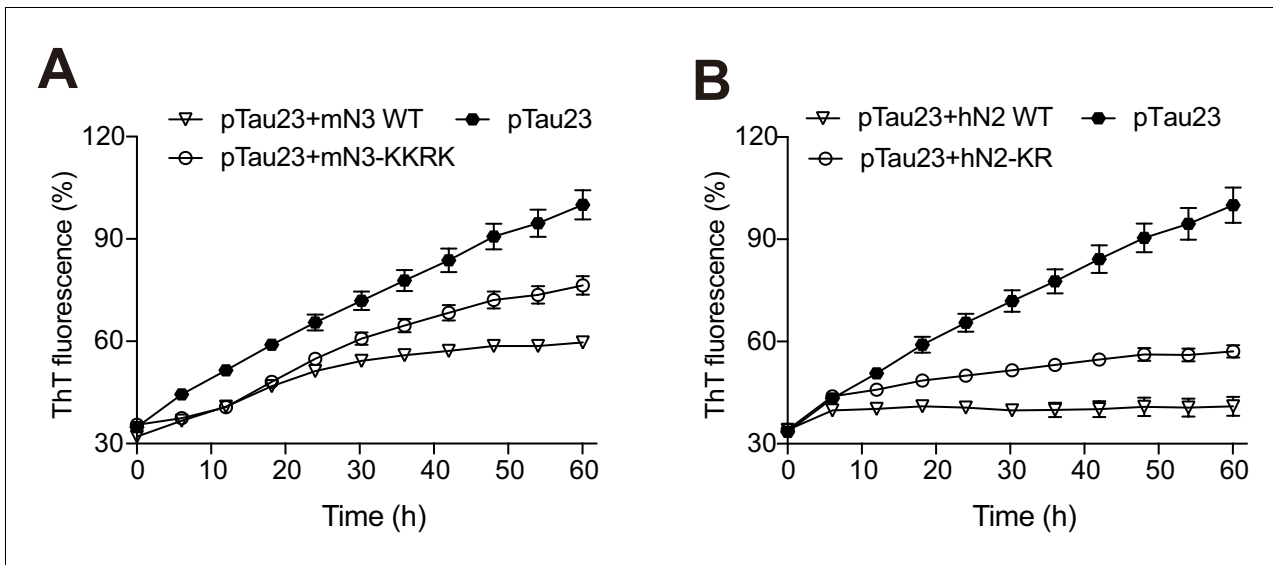


Figure 2—figure supplement 4. Influences of mN3 (A) and hN2 (B) mutations on pTau23 aggregation measured by ThT fluorescence assays. The molar ratios of mN3 and hN2 mutants to mN3 are 1:1, respectively. The data shown correspond to mean \pm s.d., with $n = 5$.

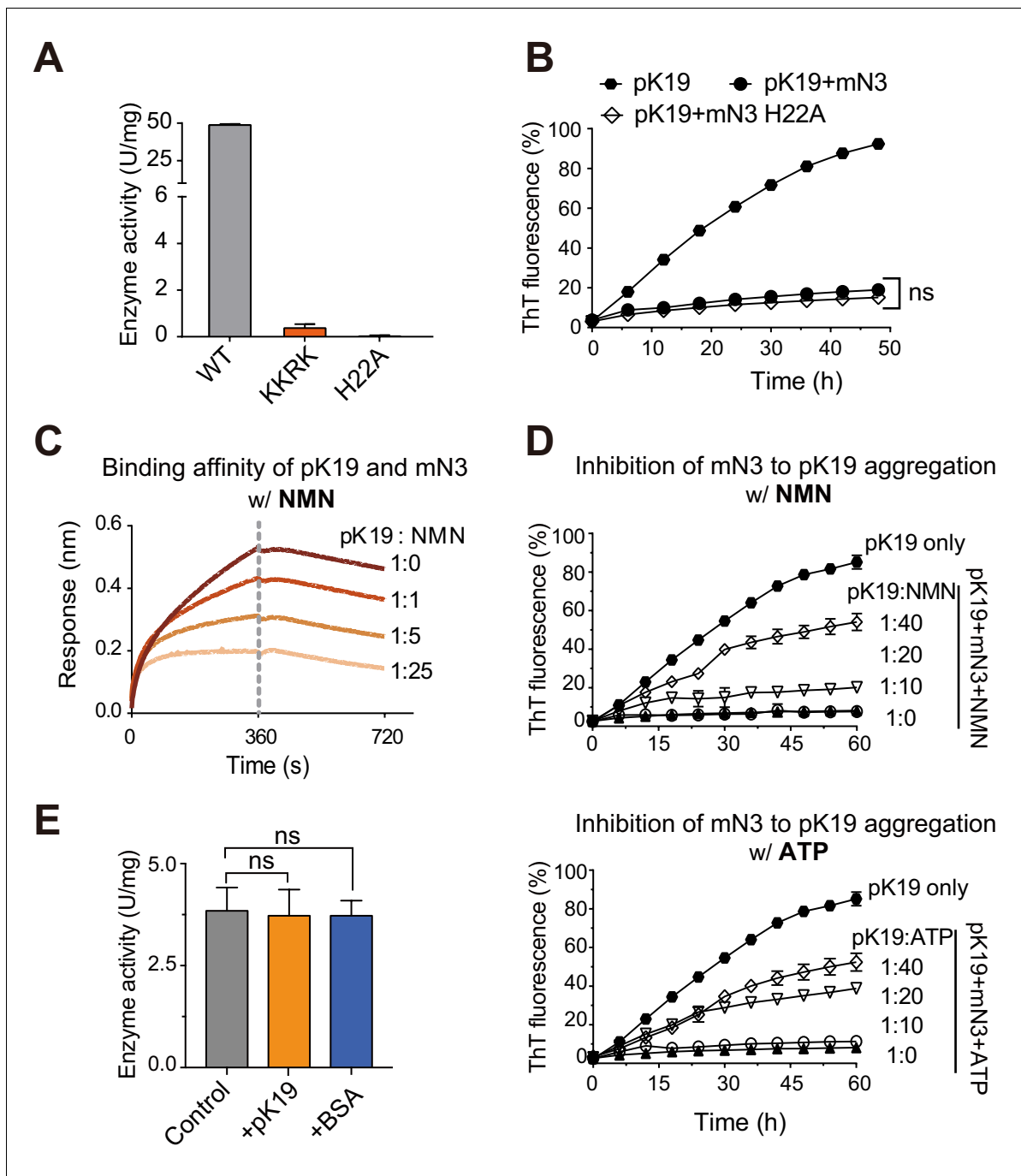


Figure 3. Competition of pK19 and NMN/ATP in the dual activities of NMNAT. (A) Enzyme activities of mN3 WT and mutants. The data showed correspond to mean \pm s.d., with $n = 3$. (B) Influence of the H22A mutation on the inhibition of mN3 against the amyloid aggregation of pK19. The molar ratio of pK19 to mN3 is 1:0.2. The data showed correspond to mean \pm s.d., with $n = 3$. Values are compared using Student's *t*-test. 'ns', not significant. (C) NMN weakens the binding of pK19 to mN3 in a dose-dependent manner measured by BLI analysis. mN3 was immobilized on the SA sensor. pK19 (50 μ M) was pre-mixed with NMN at the indicated molar ratios for association. The same amounts of NMN were used for the association and dissociation measurements. The association and dissociation profiles are divided by a vertical dash line. (D) The presence of NMN (top) or ATP (bottom) reduces the inhibitory effect of mN3 against pK19 amyloid aggregation in a dose-dependent manner. Molar ratios of pK19 to NMN/ATP are indicated. The data showed correspond to mean \pm s.d., with $n = 3$. (E) The presence of pK19 (pK19:NMN/ATP = 10:1) shows no significant influence on the enzyme activity of mN3. The data showed correspond to mean \pm s.d., with $n = 3$. Values are compared using Student's *t*-test. 'ns', not significant.

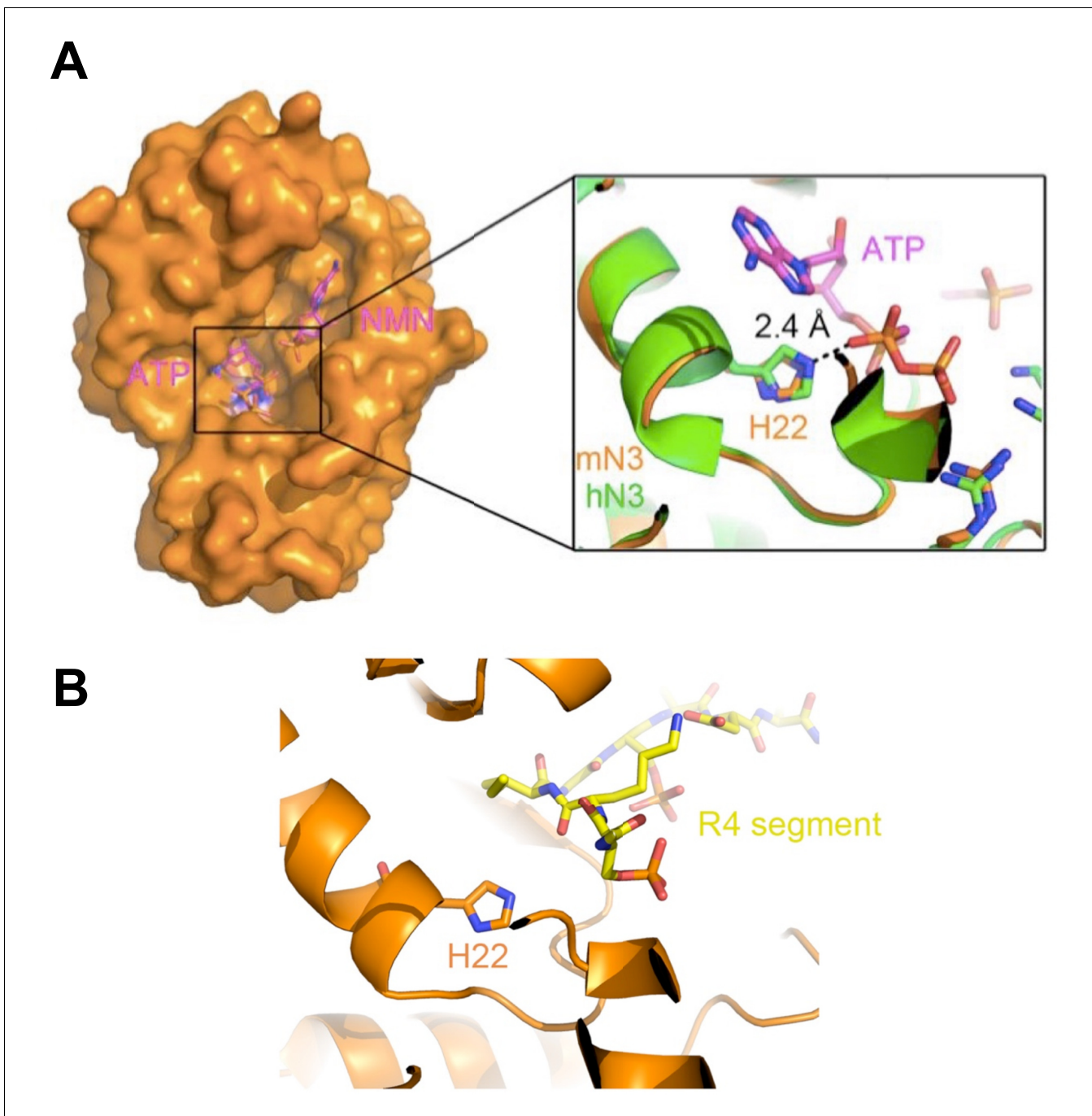


Figure 3—figure supplement 1. Position of H22 in the over-all mN3 structure. (A) The surface of the mN3 structure is shown in orange. The apo structure of mN3 is superimposed with the structure of hN3 in complex with AMP-CPP and NMN (PDB ID: 1NUS). AMP-CPP and NMN are shown in magenta as sticks. The interaction of H22 and AMP-CPP is shown in a zoom-in view. (B) R4 segment resides at the entrance of the enzymatic pocket of mN3, and thus the mutation of H22, which is deep at the bottom of the pocket, may not significantly influence the binding of R4 to mN3. R4 segment is in yellow sticks. mN3 is in orange.

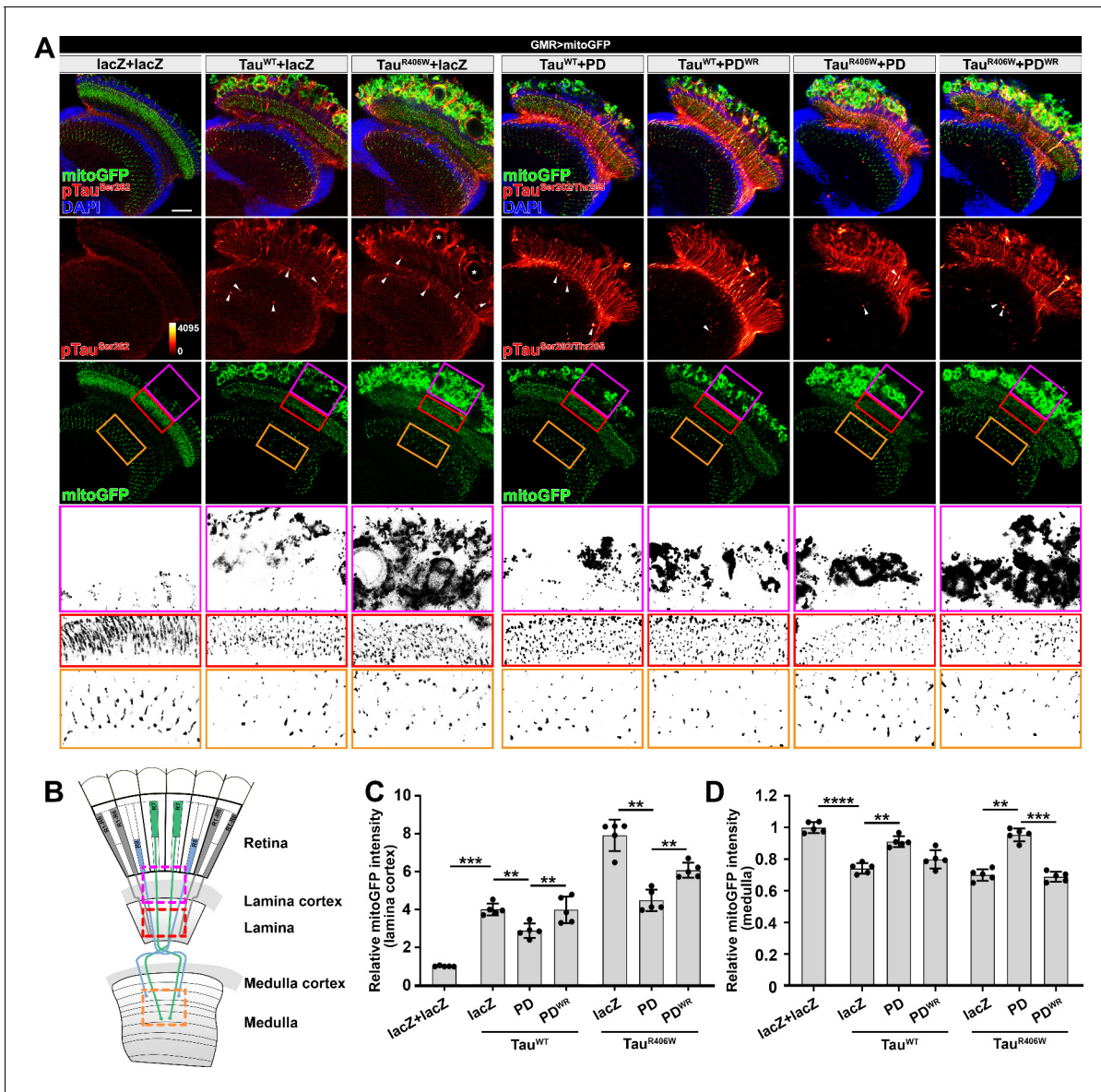


Figure 4. *Drosophila* Nmnat (PD) suppresses pTau-induced mitochondrial clustering. (A) Adult female *Drosophila* (2 days after eclosion, DAE) brains expressing mitochondrial marker mitoGFP (green) together with lacZ+lacZ, Tau^{WT}+lacZ, Tau^{R406W}+lacZ, Tau^{WT}+PD, Tau^{WT}+PD^{WR}, Tau^{R406W}+PD, or Tau^{R406W}+PD^{WR} under photoreceptor-specific driver GMR-GAL4 were stained for pTau (red spectrum) and DAPI (blue). White arrowheads show the aggregation of pTau. White asterisks show the holes formed in the lamina cortex layer, indicating retinal degeneration. Magenta, red, and yellow boxes indicate the lamina cortex, lamina, and medulla layers, respectively. Scale bar, 30 μ m. (B) Diagram of the adult *Drosophila* visual system. Each ommatidium contains six outer photoreceptors (R1–R6) and two inner photoreceptors (R7 and R8). R1–R6 traverse the lamina cortex (magenta box) and project their axons into the lamina (red box), while the axons of R7 and R8 pass through the lamina and terminate in distinct synaptic layers in the medulla (orange box). (C, D) Quantification of mitoGFP intensity in the lamina cortex (C) and medulla (D). Data are presented as mean \pm s.d., with n = 5. One-way ANOVA post hoc Tukey test; **p<0.01, ***p<0.001, ****p<0.0001.

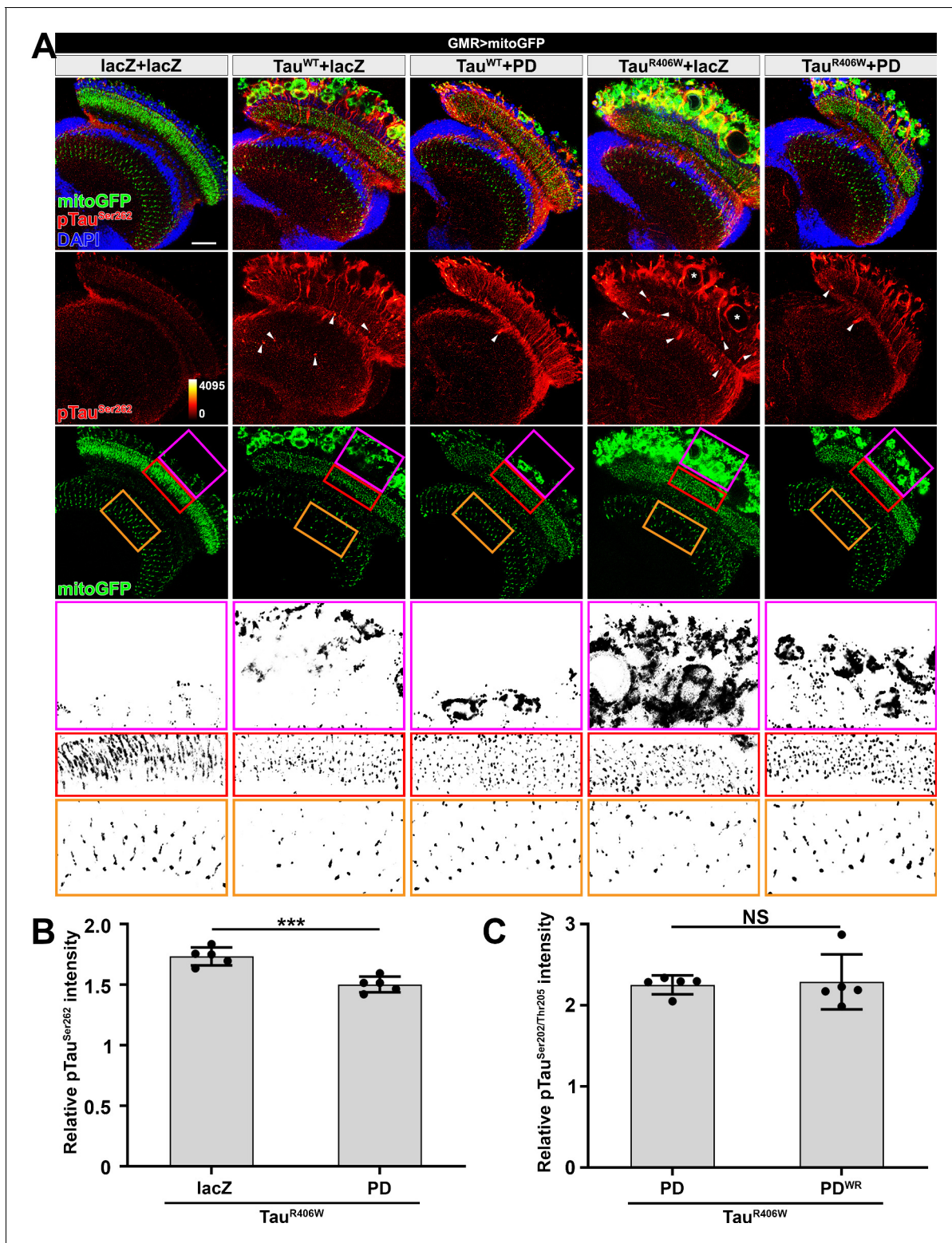


Figure 4—figure supplement 1. *Drosophila* NMNAT(PD) suppresses pTau-induced mitochondrial clustering. (A) Adult female *Drosophila* (2 DAE) brains expressing mitochondrial marker mitoGFP (green) together with lacZ+lacZ, Tau^{WT}+lacZ, Tau^{WT}+PD, Tau^{R406W}+lacZ, or Tau^{R406W}+PD under GMR-GAL4 were stained for pTau (red spectrum) and DAPI (blue). White arrowheads show the aggregation of pTau. White asterisks show the holes formed in the lamina cortex layer. Magenta, red, and yellow boxes indicate the lamina cortex, lamina, and medulla layers, respectively. Scale bar, 30 μ m. (B) Quantification of pTau^{Ser262} intensity in the lamina and lamina cortex in A. Data are presented as mean \pm s.d., with n = 5. Independent samples t-test; Figure 4—figure supplement 1 continued on next page

Figure 4—figure supplement 1 continued

*** $p < 0.001$. (C) Quantification of pTau^{Ser202/Thr205} intensity in the lamina and lamina cortex in **Figure 4A**. Data are presented as mean \pm s.d., with $n = 5$. Independent samples t-test; NS: not significant.

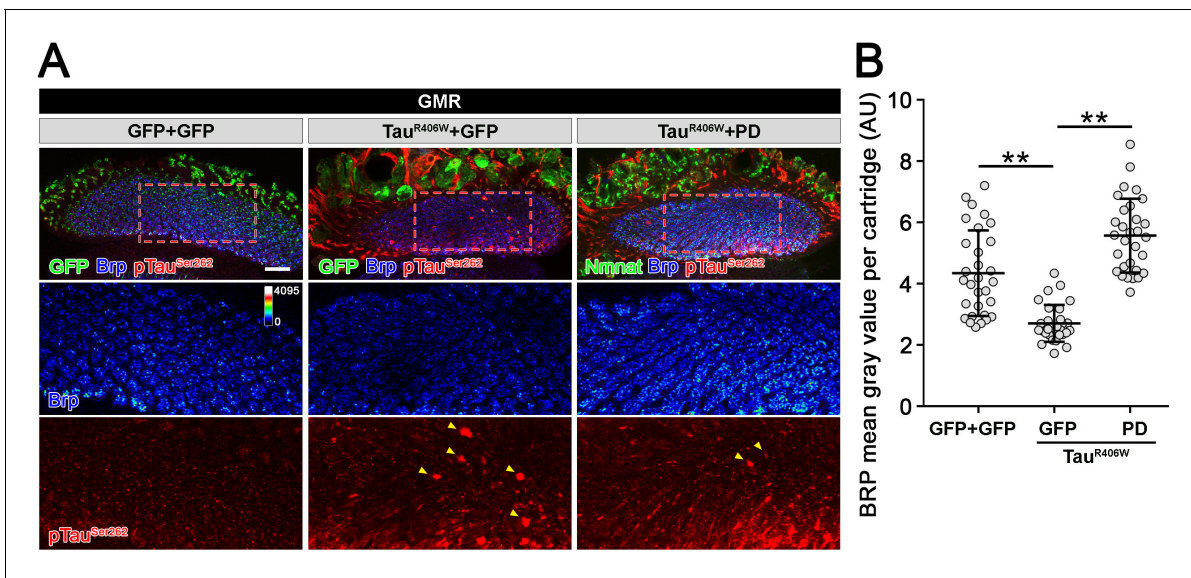


Figure 4—figure supplement 2. *Drosophila* Nmnat (PD) suppresses pTau-induced Brp loss. (A) Confocal micrographs show the Brp staining in lamina synapses. Brp labels active zone structure. pTau^{Ser262} labels hyperphosphorylated Tau. Arrowheads mark pTau aggregates. Scale bar, 20 μ m. (B) Quantification (mean \pm s.d.; n = 30 cartridges from three animals) of the Brp level in the lamina. One-way ANOVA post hoc Tukey test; **p<0.01.

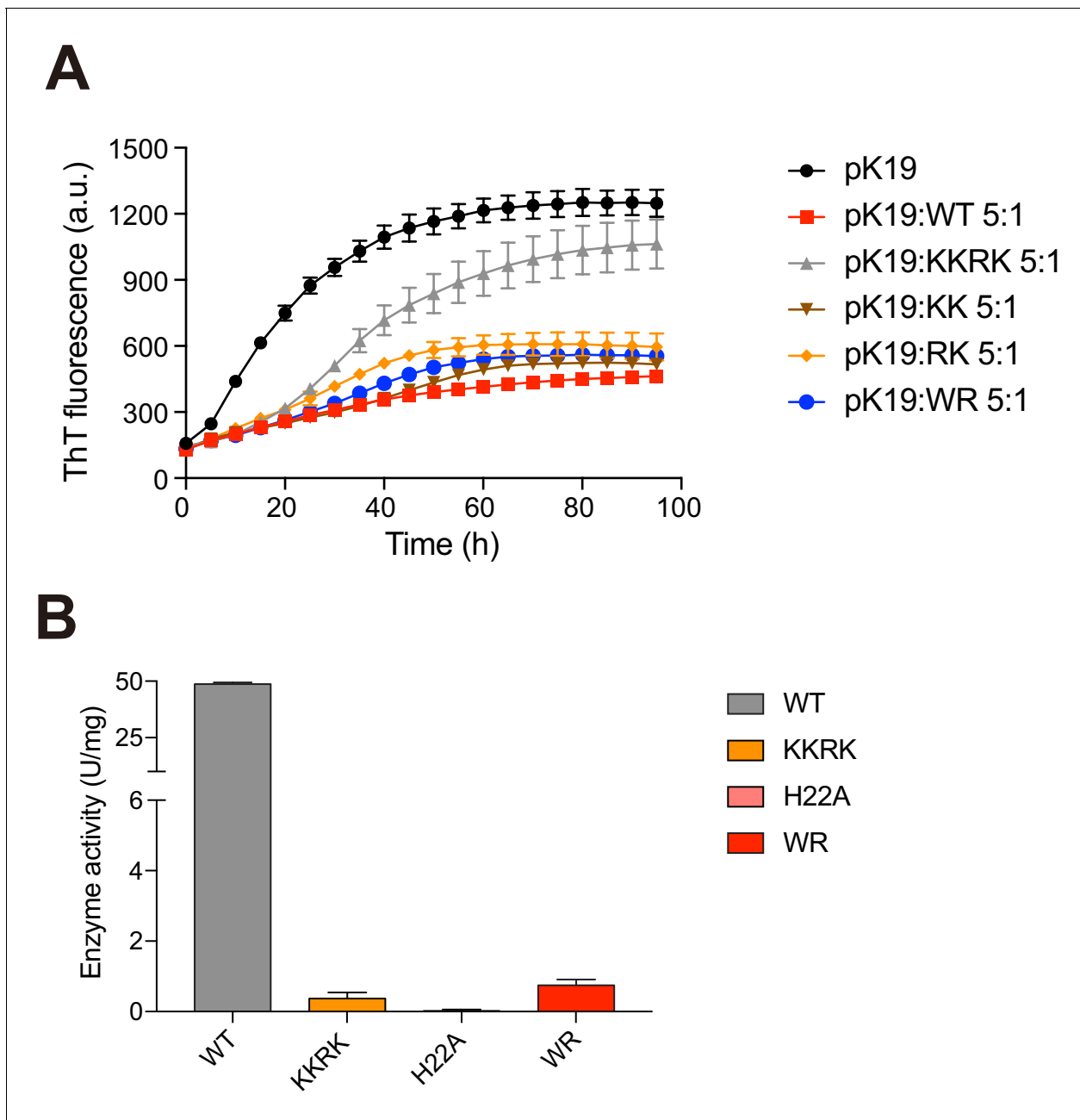


Figure 4—figure supplement 3. Activities of mN3 variants. (A) ThT fluorescence assays (top) shows the influences of mN3 mutations on the inhibition of pK19 (100 μ M) amyloid aggregation. The molar ratios of pK19 to mN3 variants are indicated. The data shown correspond to mean \pm s.d., with $n = 5$. (B) The enzymatic activities of mN3 variants measured with the NMN concentration of 625 μ M are shown below. The data shown correspond to mean \pm s.d., with $n = 3$.

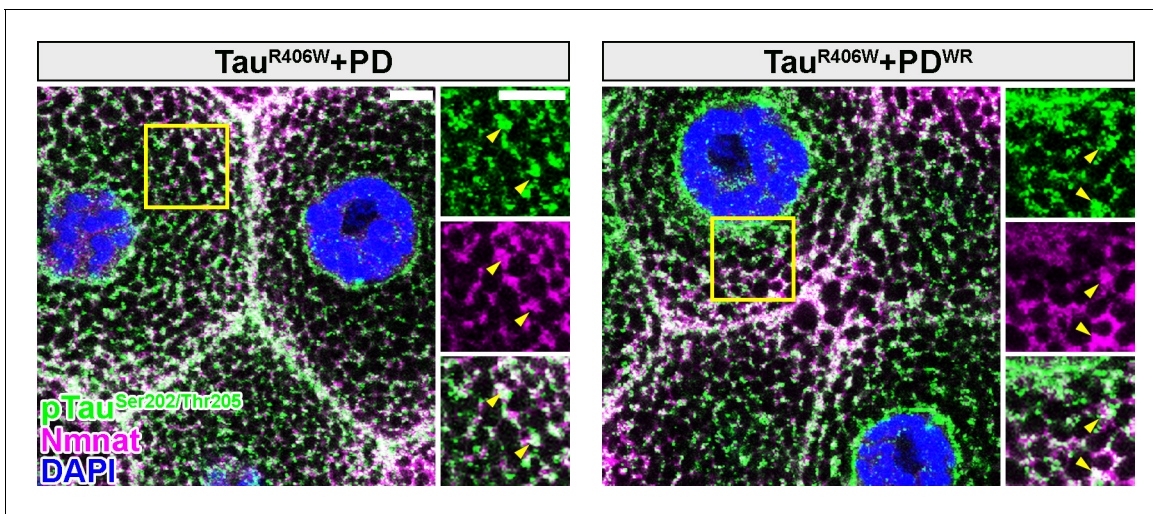


Figure 4—figure supplement 4. *Drosophila* Nmnat PD and PD^{WR} colocalize with pTau in vivo. Third instar larval salivary gland cells expressing Tau^{R406W} with PD or PD^{WR} by OK371-GAL4 were stained with pTau (green), Nmnat (magenta), and DAPI (blue). Yellow arrowheads indicate the colocalization of pTau with PD/PD^{WR}. Scale bars, 10 μ m.

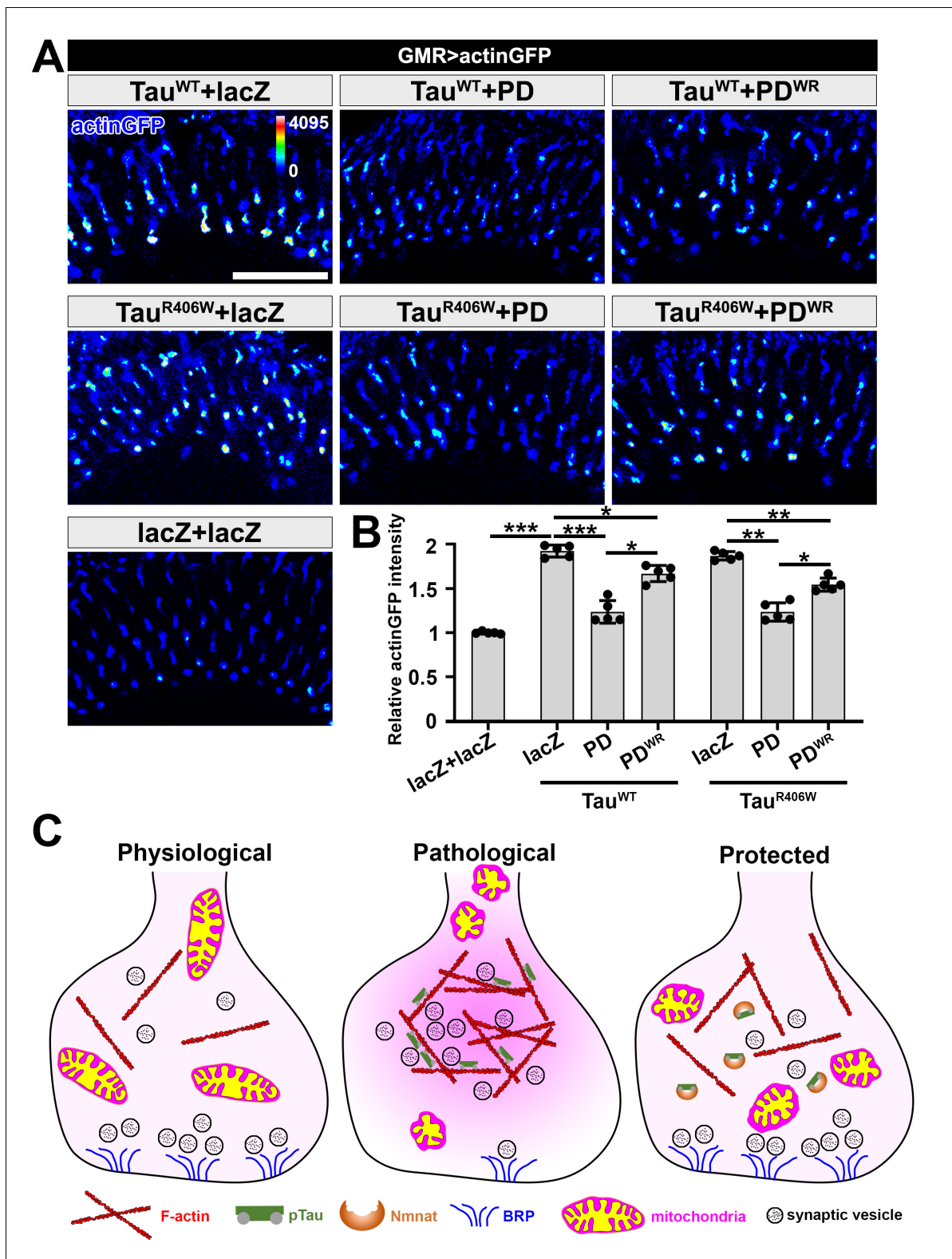


Figure 5. NMNAT (PD) suppresses F-actin accumulation at synaptic terminals. (A) Medulla area of adult female *Drosophila* (2 DAE) expressing actin-GFP (blue spectrum) together with lacZ+lacZ, Tau^{WT}+lacZ, Tau^{WT}+PD, Tau^{WT}+PD^{WR}, Tau^{R406W}+lacZ, Tau^{R406W}+PD, or Tau^{R406W}+PD^{WR} under photoreceptor-specific driver *GMR-GAL4*. Scale bar, 30 μ m. (B) Quantification of the actinGFP level in the medulla. One-way ANOVA post hoc Tukey test; * $p < 0.05$, ** $p < 0.01$, *** $p < 0.001$. (C) Schematic model of Nmnat protection against pTau-induced synaptopathy. Under pathological condition, pTau promotes mitochondrial clustering and impairs mitochondrial transport, reduces Brp level at synapses, and stimulates F-actin accumulation that

Figure 5 continued on next page

Figure 5 continued

restricts synaptic vesicle mobility. Nmnat specifically binds to pTau and regulates pTau phase separation, restores the presence of mitochondria and Brp at synaptic terminals, and alleviates F-actin accumulation.

Figure 5—figure supplement 1 continued

Tau^{R406W}+PC, or Tau^{R406W}+PD by *elav-GAL4* at 2 and 20 DAE using antibodies against pTau^{Ser262} and β -actin (internal control). (B) Quantification of the pTau levels in A. Fold change of pTau^{Ser262} was normalized to the Tau^{R406W}+GFP.nls group at 2 DAE. Data are presented as mean \pm s.d., with $n = 3$. One-way ANOVA post hoc Bonferroni's test. ** $p < 0.01$. (C) Adult yw fly brains or fly brains with neuronal expression of Tau^{R406W}+GFP.nls, Tau^{R406W}+CD8GFP, Tau^{R406W}+PC, or Tau^{R406W}+PD by *elav-GAL4* at 20 DAE were probed for Nmnat (magenta) and pTau^{Ser262} (green) and stained for DAPI (blue). In the bottom row, the intensity of pTau is indicated by a heat map. Scale bar: 50 μ m.

Figure 5—figure supplement 2 continued

Tau^{R406W}+CD8GFP, Tau^{R406W}+PC, or Tau^{R406W}+PD by *elav-GAL4* using an antibody against cleaved caspase-3. β -actin was used as an internal control. B Quantification of the cleaved caspase-3 levels in A. Fold change of P12 was normalized to 2 DAE *yw* flies. $n = 3$. Data are presented as mean \pm s.d., with $n = 3$. One-way ANOVA with Bonferroni's post hoc test. *** $p < 0.001$, NS: not significant. C Climbing performance of *yw* flies or flies with neuronal expression of CD8GFP+CD8GFP, Tau^{R406W}+GFP.nls, Tau^{R406W}+CD8GFP, Tau^{R406W}+PC, and Tau^{R406W}+PD by *elav-GAL4* at 2, 10, and 20 DAE. Ten groups (10 flies in each, total 100 flies) of each genotype were tested. Data are presented as mean \pm s.d., with $n = 10$. One-way ANOVA with Bonferroni's post hoc test. **** $p < 0.0001$, NS: not significant.

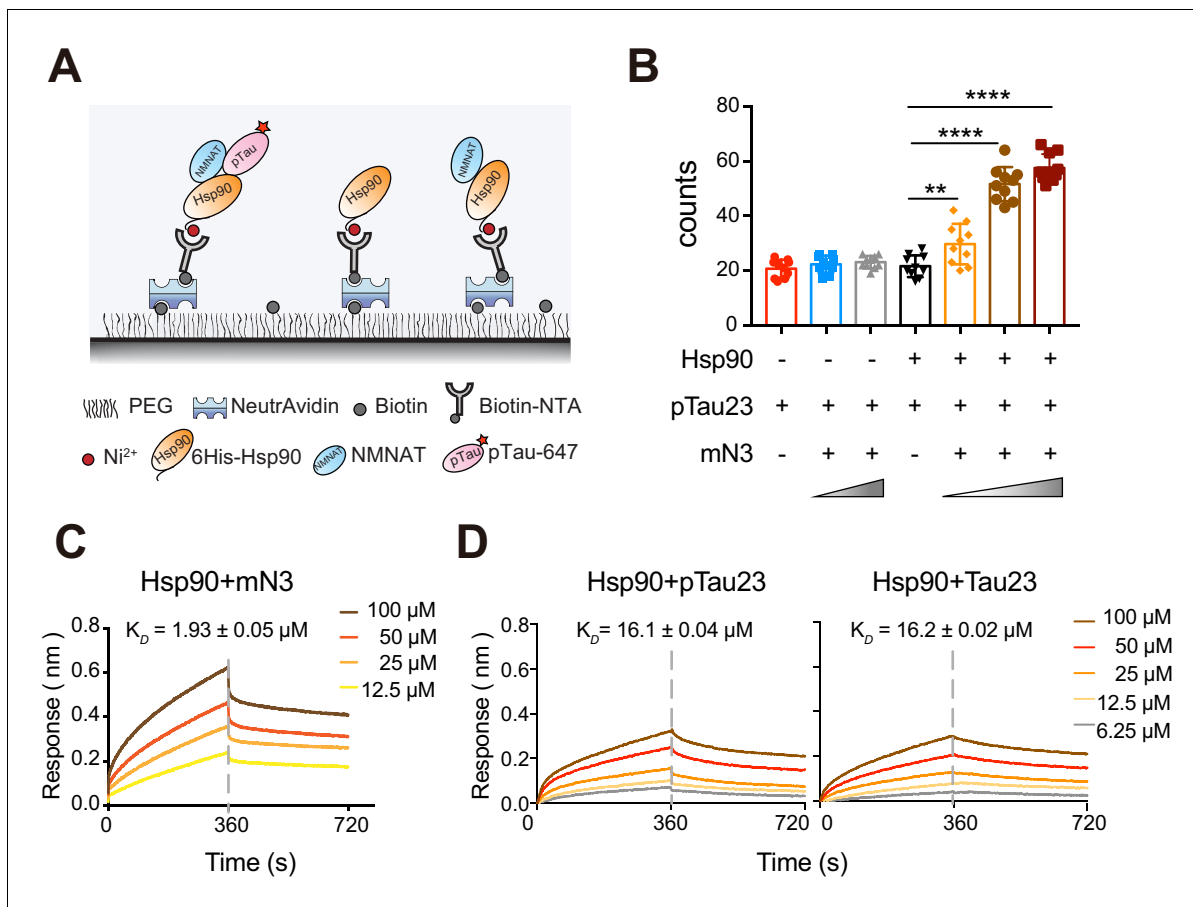


Figure 6. mN3 acts as a co-chaperone to assist Hsp90 in the recognition of pTau. (A) Schematic illustration of the SMPull assay by TIRF microscopy. His₆-tagged Hsp90 was immobilized to the slide by chelating to Biotin-NTA-Ni. Single molecular interaction was monitored by the fluorescence from Alexa-647 that was labeled on pTau23/Tau23 monomer. (B) The average number of fluorescent counts per imaging area detected by SMPull. TIRF images were recorded for the sample systems containing Hsp90, mN3 (4 nM) and pTau23 as indicated. The concentrations of mN3 from left to right are 0, 4, 20, 0, 0.8, 4, and 20 nM. Error bars denote standard deviations (s.d.) (n = 10). Values were compared using Student's *t*-test. **, *p*<0.01. ****, *p*<0.0001. (C) BLI measurements of mN3 binding to the SA sensor chip coated with biotinylated Hsp90 (20 $\mu\text{g ml}^{-1}$). The mN3 concentrations are indicated. The K_D value of mN3 binding to Hsp90 is reported. (D) BLI measurements of the binding of pTau23 (left)/Tau23 (right) to the SA sensor chip coated with biotinylated Hsp90 (20 $\mu\text{g ml}^{-1}$). The Tau protein concentrations are indicated.

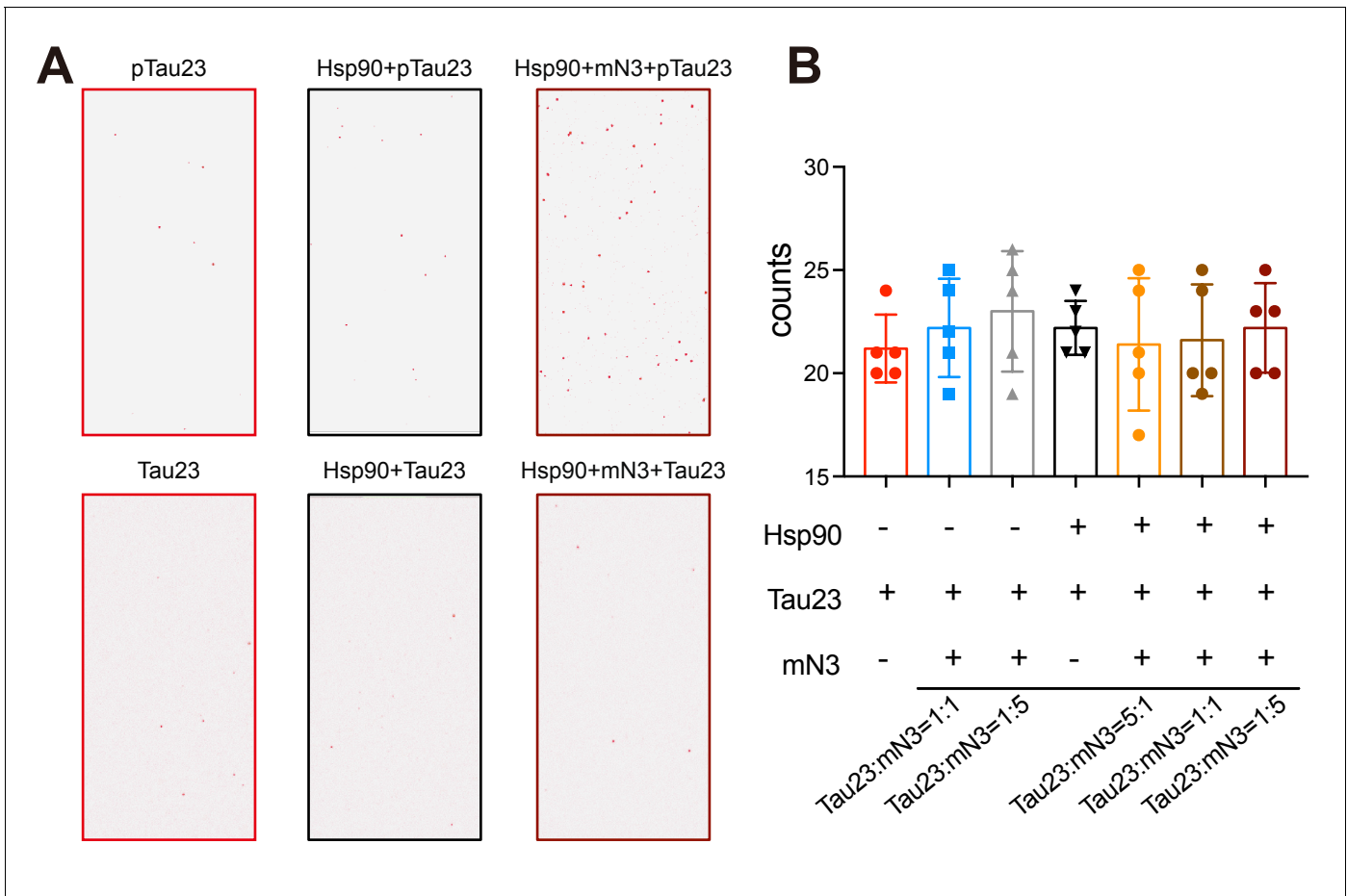


Figure 6—figure supplement 1. mN3 mediates the binding of pTau23, but not Tau23, to Hsp90. (A) TIRF microscopic images show the enhancement of mN3 to the binding of Hsp90 with pTau23 but not Tau23. (B) The average number of fluorescent counts per imaging area detected by SMPull. The concentrations of mN3 from left to right are 0, 4, 20, 0, 0.8, 4, and 20 nM. Error bars denote standard deviations (s.d.) (n = 10).

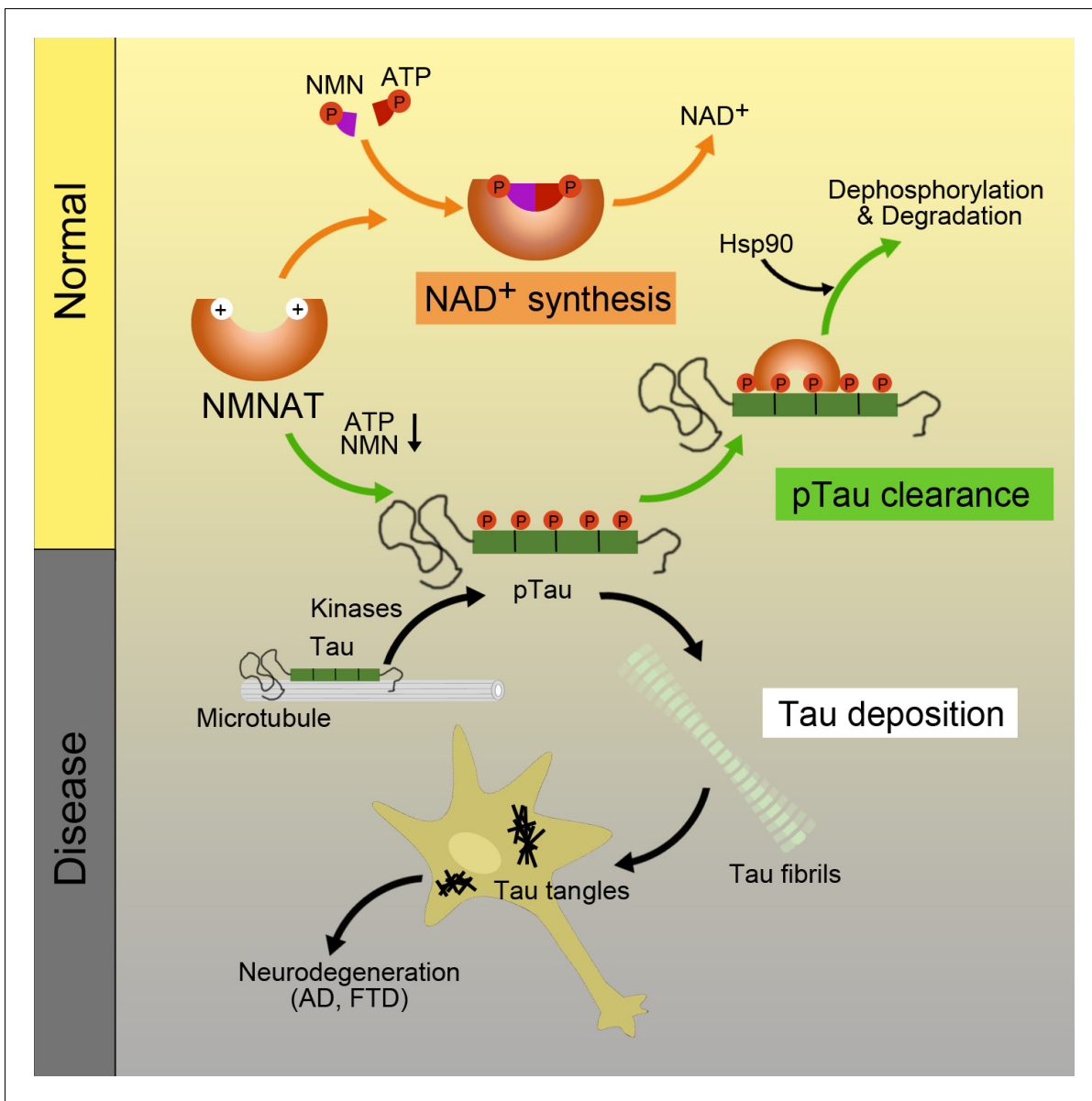


Figure 7. Schematics of NMNAT as a key node between pTau homeostasis and NAD⁺ metabolism. NMNAT functions as both an NAD⁺ synthase involved in NAD⁺ metabolism, and a chaperone-like protein assisting the clearance of pathological pTau deposition. During aging, as the levels of ATP and NMN decrease, the chaperone-like function of NMNAT may show up to antagonize pTau aggregation.